



# High-resolution and low-background $^{163}\text{Ho}$ spectrum: interpretation of the resonance tails

C. Velte<sup>1,a</sup>, F. Ahrens<sup>1</sup>, A. Barth<sup>1</sup>, K. Blaum<sup>8</sup>, M. Braß<sup>6</sup>, M. Door<sup>8</sup>, H. Dorrer<sup>2</sup>, Ch. E. Düllmann<sup>2,3,4</sup>, S. Eliseev<sup>8</sup>, C. Enss<sup>1</sup>, P. Filianin<sup>8</sup>, A. Fleischmann<sup>1</sup>, L. Gastaldo<sup>1</sup>, A. Goeggelmann<sup>7</sup>, T. Day Goodacre<sup>11,14</sup>, M. W. Haverkort<sup>6</sup>, D. Hengstler<sup>1</sup>, J. Jochum<sup>7</sup>, K. Johnston<sup>11</sup>, M. Keller<sup>1,15</sup>, S. Kempf<sup>1</sup>, T. Kieck<sup>2,5</sup>, C. M. König<sup>8</sup>, U. Köster<sup>12</sup>, K. Kromer<sup>8</sup>, F. Mantegazzini<sup>1</sup>, B. Marsh<sup>11</sup>, Yu. N. Novikov<sup>9</sup>, F. Piquemal<sup>8</sup>, C. Riccio<sup>10</sup>, D. Richter<sup>1</sup>, A. Rischka<sup>8</sup>, S. Rothe<sup>11</sup>, R. X. Schüssler<sup>8</sup>, Ch. Schweiger<sup>8</sup>, T. Stora<sup>11</sup>, M. Wegner<sup>1</sup>, K. Wendt<sup>5</sup>, M. Zampaolo<sup>10</sup>, K. Zuber<sup>13</sup>

<sup>1</sup> Kirchhoff-Institute for Physics, Heidelberg University, Heidelberg, Germany

<sup>2</sup> Institute of Nuclear Chemistry, Johannes Gutenberg University, Mainz, Germany

<sup>3</sup> GSI Helmholtzzentrum für Schwerionenforschung GmbH, Darmstadt, Germany

<sup>4</sup> Helmholtz Institute Mainz, Mainz, Germany

<sup>5</sup> Institute of Physics, Johannes Gutenberg University, Mainz, Germany

<sup>6</sup> Institute for Theoretical Physics, Heidelberg University, Heidelberg, Germany

<sup>7</sup> Physics Institute, University of Tübingen, Tübingen, Germany

<sup>8</sup> Max-Planck-Institut für Kernphysik, Heidelberg, Germany

<sup>9</sup> Petersburg Nuclear Physics Institute, Gatchina, Russia

<sup>10</sup> Laboratoire Souterrain de Modane, Modane, France

<sup>11</sup> Physics Department, CERN, Geneva, Switzerland

<sup>12</sup> Institut Laue-Langevin, Grenoble, France

<sup>13</sup> Institute of Nuclear and Particle Physics, Dresden University, Dresden, Germany

<sup>14</sup> Present address: TRIUMF, Wesbrook Mall, Vancouver, Canada

<sup>15</sup> Present address: Institut für Technische Informatik, Heidelberg University, Heidelberg, Germany

Received: 8 September 2019 / Accepted: 26 November 2019 / Published online: 21 December 2019

© The Author(s) 2019

**Abstract** The determination of the effective electron neutrino mass via kinematic analysis of beta and electron capture spectra is considered to be model-independent since it relies on energy and momentum conservation. At the same time the precise description of the expected spectrum goes beyond the simple phase space term. In particular for electron capture processes, many-body electron-electron interactions lead to additional structures besides the main resonances in calorimetrically measured spectra. A precise description of the  $^{163}\text{Ho}$  spectrum is fundamental for understanding the impact of low intensity structures at the endpoint region where a finite neutrino mass affects the shape most strongly. We present a low-background and high-energy resolution measurement of the  $^{163}\text{Ho}$  spectrum obtained in the framework of the ECHo experiment. We study the line shape of the main resonances and multiplets with intensities spanning three orders of magnitude. We discuss the need to introduce an asymmetric line shape contribution due to Auger–Meitner decay of states above the auto-ionisation threshold. With this we determine an enhancement of count rate at the

endpoint region of about a factor of 2, which in turn leads to an equal reduction in the required exposure of the experiment to achieve a given sensitivity on the effective electron neutrino mass.

## 1 Introduction

The knowledge of the effective neutrino mass scale is one of the fundamental open questions in particle physics. Until now, only upper limits for neutrino masses could be provided [1]. The most sensitive approaches to define the neutrino mass scale are the study of the distribution of mass in the universe [2], the observation of neutrinoless double beta decay [3,4] and the analysis of the endpoint region in beta and electron capture (EC) spectra [5]. Traditionally, only this latter approach is considered to be model independent because it is based on energy and momentum conservation. In contrast, the interpretation of cosmological and astrophysical data requires the assumption of fundamental cosmological models. In case of neutrinoless double beta decay, the

<sup>a</sup> e-mail: [Clemens.Velte@kip.uni-heidelberg.de](mailto:Clemens.Velte@kip.uni-heidelberg.de)

deduction of the effective Majorana mass from the measured half-life requires the assumption of a well-defined mechanism inducing this process, for example the exchange of a light Majorana neutrino. Under this assumption, the half-life of the process can be related to the effective Majorana neutrino mass. The so-obtained values are affected by a systematic uncertainty due to the poor knowledge of the related nuclear matrix element [6]. While the analysis of beta and EC spectra is model-independent it still requires a precise understanding of the spectrum [7], since uncertainties in this respect represent a systematic error in the determination of the effective electron neutrino mass.

Currently two nuclides are used for the determination of the effective electron neutrino mass. One is  ${}^3\text{H}$  undergoing a beta decay and the other one is  ${}^{163}\text{Ho}$  undergoing an electron capture [5]. Due to the different range of released energy during the EC decay of  ${}^{163}\text{Ho}$  with  $Q_{\text{EC}} = 2.8\text{ keV}$  and the beta decay of  ${}^3\text{H}$  with  $Q_{\beta} = 18.6\text{ keV}$  different techniques are required for a high precision measurement of the energy spectra. In case of  ${}^3\text{H}$ , both electron spectroscopy [8] and cyclotron radiation emission spectroscopy [9] are used to ensure an energy resolution in the eV range. In the case of  ${}^{163}\text{Ho}$ , low temperature detectors performing calorimetric measurements are used to achieve an energy resolution of a few eV.  ${}^3\text{H}$ -based experiments, in which molecular  ${}^3\text{H}_2$  is currently used, have a systematic error due to the description of final states in which daughter  ${}^3\text{He}$ - ${}^3\text{H}$  molecules are left after the decay [10]. The most stringent limit from such a kinematic measurement on the effective anti-electron neutrino mass is given by  $m_{\bar{\nu}_e} < 1.1\text{ eV}$  90% C.L. [11] achieved by the KATRIN collaboration.  ${}^{163}\text{Ho}$ -based experiments are affected by the imprecise knowledge of electron-electron scattering processes occurring in the atom during EC [7]. The present work was performed within the Electron Capture in  ${}^{163}\text{Ho}$  (ECHO) experiment [12]. The ECHO experiment has been conceived to achieve sub-eV sensitivity on the electron neutrino mass by analyzing the endpoint region of a high-statistics and high-resolution  ${}^{163}\text{Ho}$  spectrum. The main idea behind this experiment was already proposed by DeRujula [13] and comprises of performing calorimetric measurements of the  ${}^{163}\text{Ho}$  spectrum. This can be achieved if the  ${}^{163}\text{Ho}$  source is fully contained in detectors providing a 100% detection efficiency for all radiation emitted in the EC process besides the electron neutrino. The de-excitation of the daughter  ${}^{163}\text{Dy}$  atom leads mainly to the emission of Auger electrons. For an excited state following the capture of a 3s electron the branching ratio for the emission of photons is estimated to be about 0.1% [13]. The idea of a calorimetric measurement was followed by two more experiments, the HOLMES experiment [14] and NuMECS [15].

So far theoretical models could only be compared to spectra with moderate energy resolution and/or with substantial background [7, 16–20]. We present a new measurement of

the  ${}^{163}\text{Ho}$  spectrum characterized by an unprecedentedly low background, an energy resolution comparable to previous measurements [21] and an increase of the number of acquired events in the  ${}^{163}\text{Ho}$  spectrum by a factor of 2 compared to previous measurements in Fig. 1a. Here 275000 events are shown. We have a background-determined threshold of 250 eV. For the first time, this allowed us to precisely study the line shape of the resonances. In particular, we were able to analyze the part of the spectrum in the region between the two main resonance groups, that is between 440 eV and 1700 eV. The understanding of the processes required for the description of the low intensity part of the spectrum allows us to predict the shape of the spectrum in the higher-energy part below the end point region.

## 2 Experimental methods

In ECHO, the  ${}^{163}\text{Ho}$  source is enclosed in large arrays of metallic magnetic calorimeters (MMCs) [22]. These detectors are based on the calorimetric principle, where a deposition of energy in the detector leads to a temperature increase. In case of MMCs, a paramagnetic temperature sensor placed in a constant magnetic field changes its magnetization following temperature changes of the detector. This change of magnetization in turn leads to a change of magnetic flux in a low-noise high-bandwidth DC-SQUID,<sup>1</sup> which is a flux to voltage converter. The output voltage signal is proportional to the deposited energy. MMCs have shown performances which make them suitable for the ECHO experiment [23].

The results discussed here have been obtained by operating 4 pixels of a 16-pixel MMC array of the maXs-20 series for 4 days. The maXs-20 detector chip consists of a 1D array with 16 pixels. Pixels are connected gradiometrically in pairs [24]. The gradiometric design works as polarity coding for the acquired signal. This way, one readout chain can be used for 2 pixels. In addition the gradiometer makes the MMC fairly insensitive to global temperature changes of the detector chip.

The  ${}^{163}\text{Ho}$  source was embedded into each pixel of the maXs-20 detector chip in an ion implantation process at ISOLDE, CERN [25] using a mass selected ion beam [26]. The sample used to produce this source was a small amount of a chemically ultra pure  ${}^{163}\text{Ho}$  sample [27]. It was obtained by chemically separating the Ho fraction from an enriched  ${}^{162}\text{Er}$  target which was neutron irradiated at the nuclear research reactor at the Institut Laue-Langevin in Grenoble [27]. To reach a  $4\pi$  encapsulation of the  ${}^{163}\text{Ho}$ , an implantation area of  $150\text{ }\mu\text{m} \times 150\text{ }\mu\text{m}$  was defined using a photo resist mask over the two gold absorbers of the detectors, which each have dimensions of  $180\text{ }\mu\text{m} \times 180\text{ }\mu\text{m} \times 5\text{ }\mu\text{m}$  [28].

<sup>1</sup> Direct Current – Superconducting Quantum Interference Device.

After implantation and after removing the protecting photo resist layer, a second gold layer with dimensions  $175 \mu\text{m} \times 175 \mu\text{m} \times 5 \mu\text{m}$  was deposited on top of the first part of the absorber in a second photo-lithographic process. This geometry ensures that only a fraction as small as  $10^{-9}$  of the  $^{163}\text{Ho}$  decays would suffer from energy losses. This number is calculated by determining the survival probability of  $10^7$  photons with an energy distribution corresponding to the  $^{163}\text{Ho}$ -spectrum, in the given detector geometry, and in the energy interval between 1.8 keV and 3 keV where the majority of the photon loss is expected. The loss probability integrated over this interval with a 5 eV binning is in the order of  $10^{-5}$  for photons. With a branching ratio for photons of  $10^{-4}$  for each decay of  $^{163}\text{Ho}$ , the total loss probability for an event is in the order of  $10^{-9}$ .

The detectors used in this experiment have been read out using a standard 2-stage SQUID set-up [29]. Each detector of the maXs-20 array is connected via aluminium bonding wires to a DC-SQUID. One detector chip and two SQUID chips each hosting four SQUIDs [30] are positioned on the same copper holder. The output signal of each front-end SQUID is then amplified by the second SQUID stage, consisting of a low-noise SQUID array amplifier also operated at 20 mK and spatially separated from the detector. The connection between front-end SQUIDs and amplifier SQUID arrays was done using superconducting wires of NbTi in a CuNi matrix. To avoid electromagnetic disturbances coupling into the experiment, superconducting aluminium foil was wrapped around the shield connected to the 700 mK stage of the refrigerator. The SQUID systems were then read out using SQUID electronics [31] operated at room temperature.

The signal was recorded by two 16-channel digitizer cards [32] with a maximum sampling rate of 125 MHz and 16 bit. Each signal was acquired using an automated trigger. A time trace of 2.62144 ms (16384 samples with 100 MHz sampling rate and an oversampling rate of 16) was saved. The first quarter of each time window was used for pre-trigger samples, which allow us to determine the starting conditions of each signal. The last three quarters of the time window correspond to the signal time trace.

The dry dilution refrigerator which is used to reach the optimal operating temperature for the MMC array of about 20 mK was operated in the underground laboratory in Modane (Laboratoire Souterrain de Modane LSM), France [33]. No additional passive or active shielding against natural radioactivity was applied and no careful selection of the material with respect to natural activity content was performed for the detector set-up. With this experiment we were able to test the operation conditions of a set-up suitable for future ECHO experiments in an underground environment and found that no particular issues are present. We could show, by comparing the performance of detectors operated underground

with the same system operated in a laboratory above ground [28], that no degradation of detector response and noise was observed. Thanks to this result we could perform a background study in a reduced muon flux environment (4800 m water equivalent of rock overburden).

### 3 Analysis

The shape of the acquired signal is related to the thermodynamic properties of the detector [34]. The amplitude of each pulse is directly proportional to the energy deposited in the detector absorber. To extract the energy of each event an averaged time trace, obtained by the mean of about 1000 single traces corresponding to the  $M_1$  line at 2040 eV, is compared to each acquired signal with the relative amplitude as free fit parameter. This time domain template fit provides the relative amplitude of each trace with respect to the reference pulse and the mean of the quadratic distance between the time trace and the average ( $\chi^2$ -value), which indicates how much the analyzed pulse differs from the reference pulse. In addition, several parameters, which can be extracted from each signal, as the rise time, the mean of pre-trigger samples and the area underneath the signal are determined for further analysis.

The pre-trigger mean value (PTO) jumps between stable values representing stable working points of the SQUID, which are characterized by different gain. Therefore, time periods showing similar stable PTO values are combined and analyzed separately.

The data is then further analyzed to identify and eliminate signals which strongly deviate from the reference pulse. This can be achieved by applying a cut in the plane showing  $\chi^2$ -values vs. relative amplitude. The plot in Fig. 1b shows the  $\chi^2$ -values as function of the relative amplitude of the pulses (relative change of temperature of the detector) given in arbitrary units for one of the sub-files. The orange lines in this plot represent the cut on the  $\chi^2$ -values and are obtained after defining a  $5 - \sigma$  band around the centroid (red line). The goodness of this cut can be judged by looking at the histogram of the  $\chi^2$ -values shown in Fig. 1c. This way about 99% of the data is kept. All traces in the selected  $\chi^2$ -region have the same shape. This can be seen in Fig. 1d where three pulses corresponding to three different amplitudes/energies, which are marked with colored circles in Fig. 1b, are normalized and compared. The average trace is also superimposed and the precise matching of the shape can be judged for all the three pulses. On the other hand, Fig. 1e shows one of the traces eliminated by the  $\chi^2$ -cut. Here a second pulse with a different polarity occurred on the same read out channel during the acquisition of the first triggered one. The extracted scaling factor for the template fit is therefore too small for the first pulse to minimize  $\chi^2$ . The overlaid scaled average trace is clearly indicating the difference in shape.

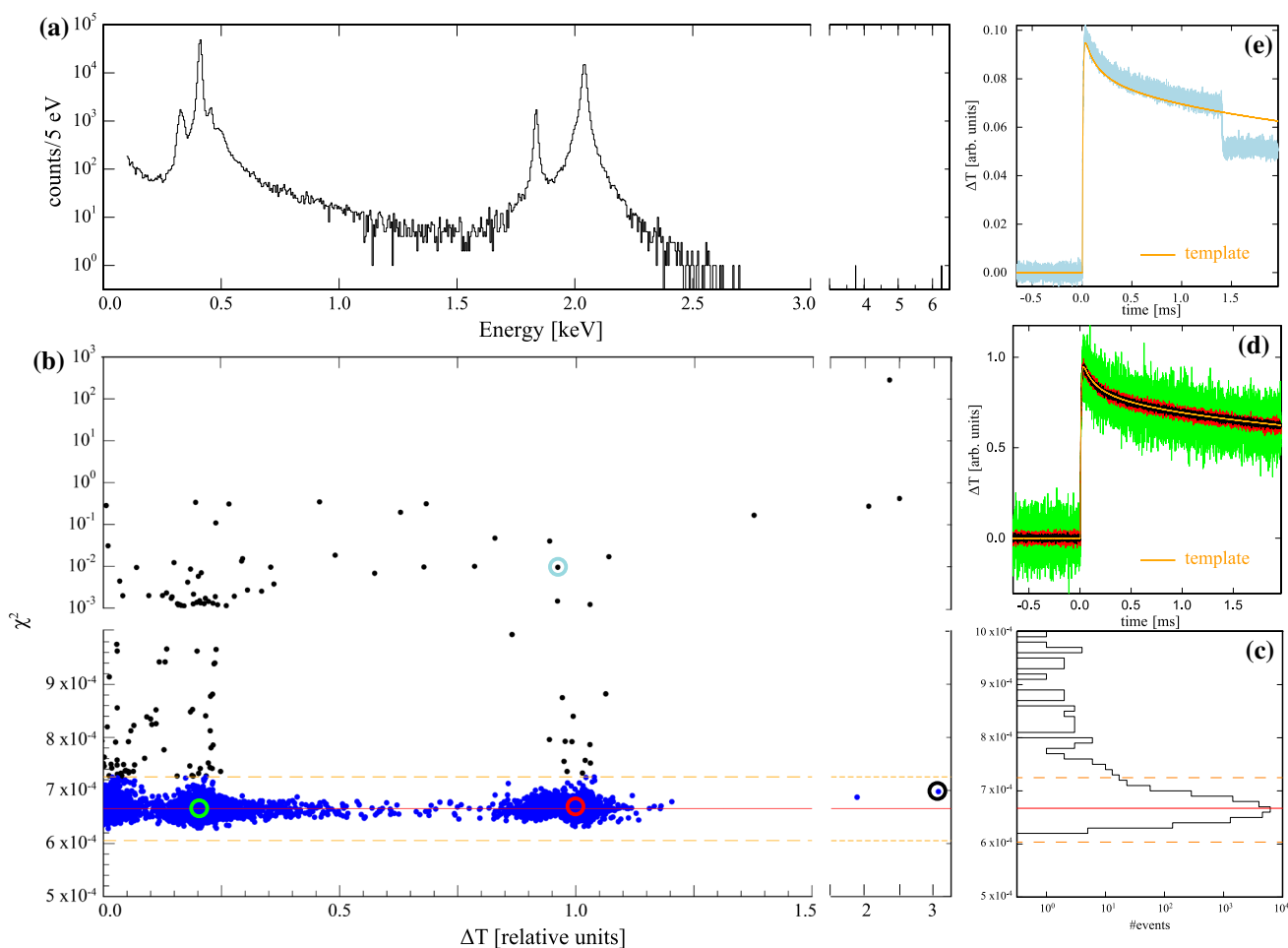


**Fig. 1** **a** Energy spectrum of the  $^{163}\text{Ho}$  decay. **b**  $\chi^2$ -value of the template fit versus the relative temperature change of the pulses. **c** Histogram of the  $\chi^2$ -values for the corresponding range in **b**. **d** 3 time traces with different absolute amplitudes and the used template scaled

to 1. The colors match the corresponding circles in plot **b**. **e** Time trace of a triggered signal with a relatively high  $\chi^2$ -value (light blue circle in **b**). Overlaid is the used template for the template fit

In a next step the data is corrected for a global temperature drift of the experimental setup in the order of  $\approx 0.5$  mK. This drift leads to a very small, but still measurable drift of the PTO, which occurs due to a minimal asymmetry of the double meander design. Therefore, by correlating the relative amplitude of the traces with the PTO we can perform a relative amplitude correction due to temperature variation.

At this point we perform the energy calibration of the  $^{163}\text{Ho}$  spectrum using the very good knowledge of the energy position of the main resonances based on a previous experiment [21]. The resulting  $^{163}\text{Ho}$  spectrum is shown in Fig. 1a and contains about 275000 counts.

An energy resolution of  $\Delta E_{\text{FWHM}} = 9.2$  eV was obtained from a fit of the  $N_1$  line using a Voigt function in which the Gaussian detector response was convoluted with a Lorentzian resonance centered at 411 eV with a width of 5.4 eV [35].

From the number of events in the  $M_1$  resonance line we extracted a mean activity of 0.18 Bq per pixel.

A crucial parameter that needs to be considered for the analysis of the  $^{163}\text{Ho}$  spectrum is the background level. Due to the fact that different SQUID working points manifested over the full acquisition time the energy range we considered for the determination of the background level was limited to a maximum value of 6.8 keV. In this energy range each working point of the corresponding signal fits the ADC voltage window. We used the window between 2.84 keV, just above the  $Q$ -value and 6.8 keV as region of interest (ROI) for the study of the background level.

In this ROI 80 events were present before applying the cuts. Among those, 78 events had a strong deviation in shape with respect to the reference pulse and therefore could be eliminated using a cut based on the  $\chi^2$  parameter. At this point, 2 events were left in the energy window between

2.84 keV and 6.8 keV, one at 3.742 keV and one at 6.250 keV, see Fig. 1a. Generally we expect two types of sources for background events: unresolved pile-up events, dependent on detector activity and time resolution, and natural radioactivity. The unresolved pile-up spectrum has the shape of the auto convoluted  $^{163}\text{Ho}$  spectrum and is therefore extending to  $2 \times Q_{\text{EC}}$ . The fraction  $f_{\text{pu}}$  of  $^{163}\text{Ho}$  decays leading to unresolved pile-up events is given in first approximation by  $f_{\text{pu}} = a \times \tau$ , where  $a$  is the activity per pixel and  $\tau$  the rise time of the signal which represents in good approximation the time resolution. In the case of the discussed experiment  $a = 0.18 \text{ Bq}$  and  $\tau = 20 \mu\text{s}$  which leads to  $f_{\text{pu}} = 3.6 \times 10^{-6}$ . So for  $2.75 \times 10^5$  counts in the total spectrum, we expect 1 count over the whole unresolved pile-up spectrum. The number of events expected in the analyzed region due to unresolved pile-up would be 0.12 which might be seen in the measured spectrum with the 1 count at  $E = 3.742 \text{ keV}$ . The remaining event can be related to natural radioactivity from the environment since the contribution due to the cosmic muon flux is negligible, being  $10^6$  times smaller with respect to the one at sea level. We calculated the background index due to environmental radioactivity by considering as worst case both events above 2.84 keV and found  $b \leq 1.6 \times 10^{-4} \text{ events/pixel/eV/day}$  95% C.L.. If we assume a constant background also in the region below 2.84 keV, then the expected number of background counts in this energy region is  $\approx 1.5$  counts versus 275000 counts in the total spectrum. This  $\approx 1.5$  counts do not have any impact on the spectral shape due to the relatively large number of counts per energy bin, which allows for a precise investigation of the  $^{163}\text{Ho}$  spectrum.

#### 4 Line-shape asymmetry

In the early days a simplified theory was used to describe the  $^{163}\text{Ho}$  spectrum in which only the main resonances were considered [13]. High-precision measurements of the  $^{163}\text{Ho}$  spectrum performed by the ECHO collaboration [12, 35] and by the NuMECS collaboration [15] have already shown that additional structures appear in the measured spectra which cannot be described by this simplified theory. Several authors have proposed more sophisticated models to describe the  $^{163}\text{Ho}$  spectra including shake-up and shake-off processes treating the Coulomb interaction on a mean-field level [16–20, 36] or using full many-body calculations [7], with improved but still modest agreement with experimental data.

From other core level spectroscopies such as core level photo-emission or X-ray absorption it is well-known that additional peaks and structures should be expected, referred to either as shake-up and shake-off states or different multiplets of the excited atom. Electrons from occupied orbitals

can scatter into previously unoccupied orbitals, due to the Coulomb interaction with the created core hole. This leads to a scenario where not just the captured, but all electrons participate in the nuclear decay. For the case where the electrons scatter into unbound orbitals this process is known as the Auger–Meitner decay, which leads approximately to an asymmetric Mahan line-shape broadening of the local atomic multiplets. This line-shape is characterized by two additional parameters compared to a Lorentzian, with  $\alpha$  representing the asymmetry of the line, and  $\xi$  a cut-off frequency related to the maximum energy a free electron can have [37–42]:

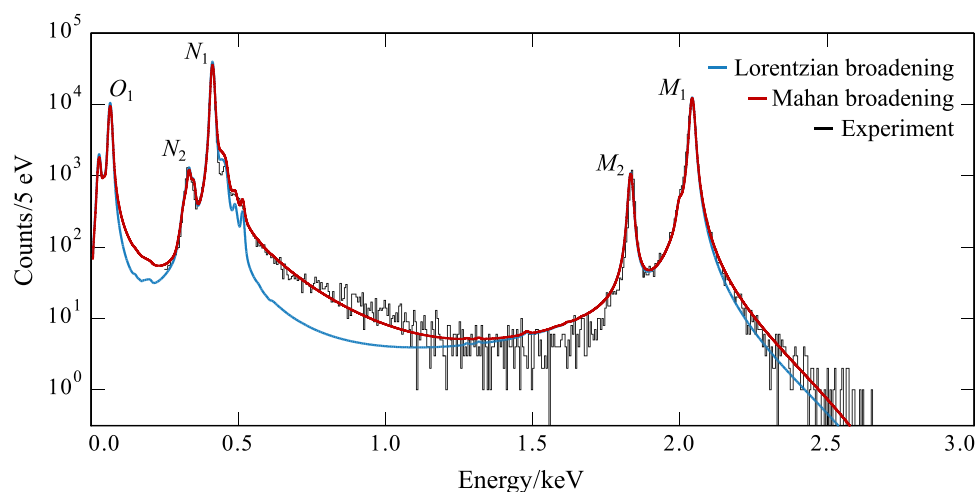
$$M(E) = \int_0^\infty L(E - E') \frac{1}{\xi \Gamma(\alpha)} \frac{e^{-E'/\xi}}{(E'/\xi)^{1-\alpha}} dE', \quad (1)$$

with  $L(E)$  a Lorentzian function centered around  $E_0$  with symmetric line width  $\Gamma$

$$L(E) = -\frac{1}{\pi} \text{Im} \left[ \frac{1}{E - E_0 + i\Gamma/2} \right]. \quad (2)$$

In Fig. 2 we show the experimental spectrum by a black histogram. Four main resonances related to the electron capture of the  $3s$  ( $M_1$ ),  $4s$  ( $N_1$ ),  $3p_{1/2}$  ( $M_2$ ) and  $4p_{1/2}$  ( $N_2$ ) spin-orbitals are clearly identifiable. On the high energy side of the  $N_1$  resonance a set of shoulders can be seen. These peaks are due to a process involving the same Coulomb interaction diagrams as responsible for the classical Auger–Meitner interaction, but now involving only bound orbitals. They arise when a  $4s$  electron is captured followed by a decay of a  $4p$  and  $4d$  electron into the  $4s$  core hole and  $4f$  partially occupied valence shell, respectively. As the Coulomb interaction between electrons in shells with the same principal quantum number is particularly strong, these are the most pronounced shake-up peaks seen in the spectrum [7]. Theoretically the  $M_1$ ,  $M_2$ ,  $N_1$ , and  $N_2$  edges are split by multiplets. The core hole angular momentum can couple parallel or anti-parallel to the valence  $4f$  angular momentum leading to several peaks within each edge. Experimentally with a resolution of 9.2 eV these splittings are hardly resolved. A hint of a multiplet splitting can be seen on the low energy side of the  $M_1$  edge around 2000 eV where theoretically an additional multiplet state is expected [7]. The blue and red lines in Fig. 2 show the theoretical electron capture spectrum. These curves are calculated by solving the many-body Coulomb-Dirac equations on a basis of bound orbitals for Ho in Au and  $Q_{\text{EC}} = 2838 \text{ eV}$  as an input. This  $Q$  value is extracted from comparing this data set to the theoretical integrated edge intensities as will be discussed later. We solve the many-body Dirac equation using a multi-configurational open shell description for the ground-state and a Green's function method for the electron capture spectra as previously described in [7]. The numerical methods used are implemented in the program Quanty [43].

**Fig. 2** Measured  $^{163}\text{Ho}$  nuclear decay spectrum (black) compared to ab initio theory broadened using a Lorentzian line-shape (blue) and Mahan line-shape (red)



In order to align the edge energies between theory and experiment we have shifted the theoretical spectrum by +6 eV to higher energy and stretched the energy scale of the theoretical spectra by 1%. The later shift in energy of the resonances accounts for many-body quantum fluctuations into shells not included in the configurational basis. The original, unmodified theory can be found in [7]. The theory calculations describe all major resonances and their relative intensities as well as the most pronounced multiplets.

The spectra shown in blue in Fig. 2 are broadened by a Lorentzian line-shape with a fitted full width at half maximum (FWHM) of 10 eV at the  $M$  edges and 5 eV at the  $N$  edges. All multiplets belonging to one edge are broadened with the same lifetime. We furthermore broadened the entire spectrum with a Gaussian of 9.2 eV FWHM to account for the experimental resolution. As one can clearly see the experimental intensity is higher than the theoretical intensity at the high energy side of the resonances, i.e., in the energy window from 500 eV to 1500 eV and above 2100 eV. Increasing the Lorentzian broadening even more would lead to a deviation on the low energy sides of the resonances. Especially in the range between 1500 eV to 1900 eV below the  $M_2$  edge the theory (with a broadening of 10 eV for the  $M$  edges) is already above the experiment, hinting that the Lorentzian lifetime of the  $M$  edges should be less than 10 eV and other asymmetric line shapes should be important.

In red we show in Fig. 2 the theoretical spectra broadened with a Mahan line-shape. We found  $\alpha = 0.01$  for the  $M$  edges and  $\alpha = 0.035$  for the  $N$  edges to get an optimum agreement between theory and experiment. In both cases we set the high energy cutoff parameter  $\xi = 300$  to account for a continuum cut-off above the relevant energy scale. Including an asymmetric line-shape substantially improves the agreement between theory and experiment. After an electron is captured the created core hole acts as a scattering center. It is essential to treat this scattering beyond mean-field theory

and include the possible simultaneous scattering of two electrons. The strongest scattering is not of a single electron on the changed potential after electron capture, but of two electrons by their Coulomb interaction. One electron will scatter from an occupied shallow core or valence orbital into the previously created core hole. The second electron scatters from an occupied orbital into the continuum. The energy the first electron gains by filling the core-hole is transferred to the second electron that is then emitted from the atom. These interactions are always present, but without a core-hole the process is forbidden by the Pauli principle. This Auger–Meitner process for initial states with energies above the auto ionisation threshold leads to the asymmetric line-shape as seen in the experiment.

Although the Mahan line-shape has been derived for a metal with several approximations including a constant density of states that are not perfectly realized for the Ho atom in Au, the resulting function describes the electron capture line-shape seen in the experiment reasonably well. Small deviations between theory and experiment can be found. Below the  $M$  edges, around 1600 eV, one finds the theory to be too high in intensity with respect to the experiment. This might well be due to interferences between the  $M$  edges and the tail of the  $N$  edges. Such interferences can lead to an additional Fano profile of the edges. These discrepancies might become important for an accurate determination of the line-shape in the end-point region. In order to improve the agreement between theory and experiment further it is important to explicitly include the Auger–Meitner process and include all decay channels of the bound atomic multiplets into continuum states due to Coulomb interaction as well as their inferences.

Nevertheless, the demonstrated presence of high-energy tails for the main resonances has a very positive effect for the analysis of the endpoint region of the  $^{163}\text{Ho}$  spectrum for the determination of the electron neutrino effective mass. In fact

the presence of the tail above the  $M_1$ -line has the effect of increasing the count rate in the region of the spectrum where a finite neutrino mass would leave the major imprint. In the region between 2.6 keV and 2.838 keV this new description will lead to an increase in counts of about a factor of two. This means that the targeted sensitivity for the effective electron neutrino mass will be reached in half of the planned time or with half of the planned detectors, meaning half of the exposure.

Using the results from our *ab initio* theory approach as a good description of the  $^{163}\text{Ho}$  spectrum we can extract the value of the decay energy with  $Q_{\text{EC}} = 2.838 \pm 0.014$  keV. The value has been obtained by a Bayesian parameter estimation. The integrated spectral weight contained in  $3s$ ,  $3p$  and  $4s$  plus  $4p$  resonances have been estimated each for both theory and experiment. A constant prior for  $Q_{\text{EC}}$  and a Gaussian Likelihood for the integrated spectral weights have been assumed. The Gaussian variance is given by the statistical uncertainty of the data and theoretical uncertainty which is marginalized assuming a Jeffreys prior. The resulting posterior for  $Q_{\text{EC}}$  has mean and standard deviation given above and a 95% confidence interval [2.807, 2.869] keV. The found value is in good agreement with previous determinations of  $Q_{\text{EC}} = 2.833 \pm 0.030^{\text{stat}} \pm 0.015^{\text{syst}}$  keV [44] and  $Q_{\text{EC}} = 2.843 \pm 0.009^{\text{stat}} - 0.060^{\text{syst}}$  keV [35].

The analysis of this data set by considering the Mahan fit as underlying theory and using profile log-likelihood ratio hypothesis test on the end point region of the  $^{163}\text{Ho}$  spectrum leads to a very moderate improvement on the upper limit on the effective electron neutrino mass  $m_{\nu_e} < 150$  eV 95% C.L.. The nuisance parameters were the  $Q_{\text{EC}}$ -value extracted for this data set, the detector energy resolution, the fraction of unresolved pile-up events and the background level.

## 5 Conclusions

The analysis of the endpoint region of the calorimetric measured  $^{163}\text{Ho}$  spectrum is considered to be the best approach to determine the value of the effective electron neutrino mass studying electron capture processes. To reduce the statistical uncertainties spectra with a number of events of the order of  $10^{14}$  and featuring an energy resolution of the order of 1 eV FWHM need to be acquired [12]. The reduction of the systematic errors relies on the reduction of background and on a very good understanding of the expected spectral shape. The  $^{163}\text{Ho}$  spectrum we have presented has been acquired in underground laboratories in Modane. A very low background index of  $b \leq 1.6 \times 10^{-4}$  events/pixel/eV/day 95% C.L. has been determined. This indicates that the same or an even lower background index can be achieved also at ground level by introducing active and passive muon veto together with a selection of low radioactive contamination materi-

als for the preparation of the detector set-up. The very low background in combination with the good energy resolution allowed for a detailed study of the spectral shape. Structures already proposed in [7] and present in previously measured spectra as for example in [15,35], have been confirmed. A low energy shoulder at the  $M_1$  resonance has been identified for the first time. In addition, we could for the first time precisely analyze the energy range between the two main resonance groups and confirm the presence of high energy tails in particular above the  $N_1$  and  $M_1$  lines as was already discussed in [19,20]. We presented a phenomenological description of these tails using a Mahan function which helped to estimate the enhancement of count rate in the endpoint region of the spectrum. A detailed study of these asymmetric tails including the full Auger–Meitner decay calculated on an *ab-initio* level is highly desirable. This will result in an improved understanding of the electron capture spectrum of  $^{163}\text{Ho}$  in the end-point region needed to extract a sub-eV neutrino mass.

With this we conclude that the enhancement of counts towards the endpoint of the  $^{163}\text{Ho}$  spectrum would allow for reaching a given sensitivity on the effective electron neutrino mass with half of the previously planned exposure not including these features. The analysis of the discussed set of data was used as a test bench for the analysis of the spectrum and resulted in a improved determination of  $Q_{\text{EC}} = 2.838 \pm 0.014$  keV and an upper limit for the effective electron neutrino mass of  $m_{\nu_e} < 150$  eV 95% C.L..

**Acknowledgements** The experiment described in this paper was possible thanks to the DFG Research Unit FOR 2202 Neutrino Mass Determination by Electron Capture in  $^{163}\text{Ho}$ , ECHO (funding under DU 1334/1-1, GA 2219/2-1, EN 299/7-1, JO 451/1-1, BL 981/5-1, EN 299/8-1) and was supported by the Max Planck Society and by the IMPRS-PTFS. We acknowledge the support of the clean room team of the Kirchhoff-Institute for Physics, Heidelberg University. We thank the staff of the Modane Underground Laboratory for their technical assistance in running the experiment. H. Dorrer acknowledges support by the Stufe 1 funding of the Johannes Gutenberg-University Mainz. L. Gamer and F. Mantegazzini acknowledge support by the Research Training Group HighRR (GRK 2058) funded through the Deutsche Forschungsgemeinschaft, DFG. Furthermore, this project has received funding from the European Research Council (ERC) under the European Union's Horizon 2020 research and innovation program under grant agreement No. 832848-FunI.

**Data Availability Statement** This manuscript has no associated data or the data will not be deposited. [Authors' comment: The data sets generated during and/or analysed during the current study are available from the corresponding author on reasonable request.]

**Open Access** This article is licensed under a Creative Commons Attribution 4.0 International License, which permits use, sharing, adaptation, distribution and reproduction in any medium or format, as long as you give appropriate credit to the original author(s) and the source, provide a link to the Creative Commons licence, and indicate if changes were made. The images or other third party material in this article are included in the article's Creative Commons licence, unless indicated otherwise in a credit line to the material. If material is not

included in the article's Creative Commons licence and your intended use is not permitted by statutory regulation or exceeds the permitted use, you will need to obtain permission directly from the copyright holder. To view a copy of this licence, visit <http://creativecommons.org/licenses/by/4.0/>.  
Funded by SCOAP<sup>3</sup>.

## References

1. F. Capozzi et al., Phys. Rev. D **95**, 096014 (2017)
2. M. Archidiacono et al., JCAP **2**, 52 (2017)
3. A. Gando et al., Phys. Rev. Lett. **117**, 109903 (2016)
4. M. Agostini et al., Phys. Rev. Lett. **111**, 122503 (2013)
5. G. Drexlin et al., Adv. High Energy Phys. **2013**, 293986 (2013)
6. J. Michelle et al., Annu. Rev. Nucl. Part. S. **69** (submitted for publication). [arXiv:1902.04097](https://arxiv.org/abs/1902.04097)
7. M. Braß et al., Phys. Rev. C **97**, 054620 (2018)
8. M. Aker et al., arXiv physics.ins-det, [arXiv:1909.06069](https://arxiv.org/abs/1909.06069) (2019)
9. A. Esfahani et al., Phys. Rev. C **99**, 055501 (2019)
10. L.I. Bodine, D.S. Parno, R.G.H. Robertson, Phys. Rev. C **91**, 035505 (2015)
11. M. Aker et al., arXiv hep-ex, [arXiv:1909.06048](https://arxiv.org/abs/1909.06048) (2019)
12. L. Gastaldo et al., EPJ-ST **226**, 1623 (2017)
13. A. De Rújula et al., Phys. Lett. B **118**, 429 (1982)
14. B. Alpert et al., EPJ-C **75**, 112 (2015)
15. M.P. Croce et al., J. Low Temp. Phys. **184**, 958 (2016)
16. R.G.H. Robertson, Phys. Rev. C **91**, 035504 (2015)
17. A. Faessler et al., Phys. Rev. C **91**, 045505 (2015)
18. A. Faessler et al., Phys. Rev. C **91**, 064302 (2015)
19. A. De Rújula, M. Lusignoli, J. High Energy Phys. **05**, 15 (2016)
20. A. Faessler et al., Phys. Rev. C **95**, 045502 (2017)
21. P.C.-O. Ranitzsch et al., J. Low Temp. Phys. **167**, 1004 (2012)
22. A. Fleischmann et al., Cryogenic particle detection, in *Springer Topics in Applied Physics*, vol. 99, ed. by C. Enss (Springer, Berlin, 2005)
23. S. Kempf et al., J. Low Temp. Phys. **193**, 365 (2018)
24. C. Pies et al., J. Low Temp. Phys. **167**, 269 (2012)
25. E. Kugler, Hyperfine Interact. **129**, 23 (2000)
26. L. Gastaldo et al., Nucl. Instrum. Methods A **711**, 150 (2013)
27. H. Dorrer et al., Radiochim. Acta **106**, 535 (2018)
28. C. Hassel et al., J. Low Temp. Phys. **184**, 910 (2016)
29. D. Drung et al., *NATO ASI Series E329* (Kluwer, Dordrecht, 1996)
30. D. Drung et al., IEEE Trans. Appl. Supercond. **17**, 699 (2007)
31. SQUID electronics type XXF1 from Magnicon GmbH, Hamburg
32. SIS3316 from Struck Innovative Systeme
33. <http://www.lsm.in2p3.fr/>
34. A. Fleischmann et al., J. Low Temp. Phys. **118**, 7 (2000)
35. P.C.-O. Ranitzsch et al., Phys. Rev. Lett. **119**, 122501 (2017)
36. A. Faessler et al., J. Phys. G **42**, 015108 (2015)
37. G.D. Mahan, Phys. Rev. **163**, 612 (1967)
38. S. Doniach et al., J. Phys. C **3**, 285 (1970)
39. B. Roulet et al., Phys. Rev. **178**, 1072 (1969)
40. P. Nozières et al., Phys. Rev. **178**, 1084 (1969)
41. P. Nozieres et al., Phys. Rev. **178**, 1097 (1969)
42. P.W. Anderson, Phys. Rev. Lett. **18**, 1049 (1967)
43. M.W. Haverkort, J. Phys. Conf. Ser. **712**, 012001 (2016)
44. S. Eliseev et al., Phys. Rev. Lett. **115**, 062501 (2015)